Materials Advances

ROYAL SOCIETY OF CHEMISTRY

PAPER

View Article Online
View Journal | View Issue

Cite this: *Mater. Adv.*, 2026, 7, 2716

Covalent functionalization of $MoSe_2$ nanosheets with hydrogen bond-donating functionalities for the sensing of nitroaromatics

Rabiaa Hajlaoui,[ab] Sabrine Baachaoui,[b] Sami Ben Aoun,[c] Said Ridene *[a] and Noureddine Raouafi[d]

Nitroaromatic compounds serve as indicators of environmental pollution and are specifically related to contamination by pesticides and explosive residues. Consequently, the development of sensitive sensing materials for their detection is of significant interest in environmental monitoring. This study investigates the chemical functionalization of molybdenum diselenide ($MoSe_2$) with organic halogenated groups possessing hydrogen-bonding donor functionalities (*i.e.*, $-CONH_2$, $-CO_2H$, and $-SO_3H$), with the objective of employing them as sensing materials for the detection of selected nitroaromatics, including nitrobenzene (NB), *m*-nitrotoluene (*m*-NT), *p*-nitrotoluene (*p*-NT), *p*-nitrophenol (*p*-NP), picric acid (TNP), and *p*-nitroaniline (*p*-NA). These findings indicate that the chemical tethering of functional alkyl groups enhances physical adsorption, with chemical reaction energies 100 times greater than the physical adsorption energies. Electronic properties, such as the density of states (DOS), projected DOS, and band structures, demonstrate significant alterations in conduction and bandgap modulation, with a reduction of 0.5 eV. In the presence of target molecules, high adsorption energies were observed, particularly in the range of −1.84 to −2.26 eV, notably for $MoSe_2$/**2c** bearing the $-SO_3H$ moiety. The partial charges, electronic density differences, and recovery times further corroborated the potential application of these materials in assessing pollution by nitroaromatic compounds for environmental monitoring in ecosystems.

Received 30th October 2025,
Accepted 15th January 2026

DOI: 10.1039/d5ma01255d

rsc.li/materials-advances

1. Introduction

Nitroaromatic compounds (NACs) are a significant class of organic pollutants widely used in the production of explosives, dyes, pesticides, pharmaceuticals, and fine chemicals.[1–4] They are characterized by the presence of one or several nitro groups attached to an aromatic ring, which confer high chemical stability and strong electron-withdrawing properties. After use, nitroaromatic residues persist in nature and contaminate food and water supplies. For instance, the breakdown of the widely used organophosphorus pesticide parathion yields 4-nitrophenol, which has a half-life of about 40 days under aerobic conditions and longer under anaerobic conditions and may persist in soil for 3–4 months after use.[5,6] Many researchers have made substantial progress in the detection of nitroaromatic compounds.[7–10] Nitrobenzene (NB), *m*-nitrotoluene (*m*-NT), *p*-nitrotoluene (*p*-NT), picric acid (TNP), 4-nitrophenol (*p*-NP) and *p*-nitroaniline (*p*-NA) are particularly noteworthy because of their environmental persistence, toxicity, and role in military and industrial applications.[11] For example, *p*-NA is associated with hematological, splenic, and renal toxicities and is classified as a potential Group 2B carcinogen by the IARC.[12] Even at low concentrations, NACs pose significant risks to human health by affecting the liver, blood, and nervous system and can lead to long-lasting contamination of soil and groundwater.[13,14] These hazardous effects highlight the urgent need to develop sensitive and selective sensing methods based on nanomaterials with tailored properties.[15,16]

A survey of recent literature shows that particular attention has been devoted to the design of responsive small-molecule systems for the detection of nitroaromatics such as trinitrophenol, trinitrotoluene (TNT), dinitrotoluene (DNT), dinitrobenzene (DNB), nitrobenzene, and nitrotoluene (NT).[17–19] For instance, melanin oligomers have been used to detect nitroaromatics, showing a high affinity for TNT and TNP.[17] Only a few reports have focused on the study of new materials useful for sensing nitroaromatics.[20–22] The Perdew–Burke–Ernzerhof (PBE) functional is widely used in

[a] *Advanced Materials and Quantum Phenomena Laboratory, Department of Physics, Faculty of Sciences of Tunis, Tunis El Manar University, 2092, Tunis, Tunisia. E-mail: said.ridene@fst.utm.tn*
[b] *Analytical Chemistry and Electrochemistry Lab (LR99ES15), Department of Chemistry, Faculty of Sciences of Tunis, University of Tunis El Manar, 2092, Tunis, Tunisia*
[c] *Department of Chemistry, Faculty of Science, Taibah University, P. O. Box 30002, Al-Madinah Al-Munawwarah, Saudi Arabia*
[d] *Basic and Applied Scientific Research Center (BASRC), Imam Abdulrahman Bin Faisal University, P. O. Box 1982, Dammam, 31441, Saudi Arabia*

material-based studies, illustrating its robustness in solid-state quantum simulations.[23] The interaction energy ranged between −1.1 and −2.8 eV for transition metal-modified materials[18,21] and between −0.1 and −0.7 eV for sensing materials relying on hydrogen bonding and other weak physical interactions.[18,19,24] For instance, Hashmi *et al.* used pentacarbon dinitride (C_5N_2) nanosheets for nitroaromatic detection,[25] which showed selectivity in the order TNP > TNT > DNB. Functionalized BC_3 nanosurfaces have also been used to detect various nitroaromatics.[26] Luminescent organic metal frameworks have been used to selectively detect NB in the presence of benzene and acetone.[22] C_{24}-TM materials, where TM is Sc, Cr, or Mn, showed higher interaction energies of −2.0 to −2.8 eV in the presence of nitrobenzene.[21]

Numerous 2D materials, such as graphene, MoS_2, WS_2, and other TMDs, have been studied for nitroaromatic sensing applications. Despite these encouraging instances, the detection of NACs in these systems is primarily controlled by π–π stacking and charge–transfer interactions between the conductive surface and aromatic rings, which frequently lead to limited chemical selectivity and moderate sensitivity.[27,28] Similarly, virgin, doped, or defect-engineered TMD monolayers have been used in extensive research on MoS_2 and WS_2-based sensors, where the sensing mechanism is primarily governed by physisorption and weak charge transfer effects.[29] These methods can increase the strength of adsorption, but they typically lack chemical recognition sites, which limit their selectivity towards structurally identical nitroaromatic compounds.

The conjugated aromatic structure and electron-deficient nitro groups favor charge–transfer interactions with electron-rich surfaces. These properties make NACs ideal targets for detection using nanomaterials, especially 2D materials, whose active surfaces can interact through π-stacking, dipole–dipole interactions, or hydrogen bonding.[25,30] However, pristine 2D materials, such as transition metal dichalcogenides, have limited chemical reactivity and reduced adsorption efficiency and selectivity towards complex molecules, such as NACs.[31] To enhance the sensing performance, surface functionalization strategies, including covalent and non-covalent approaches, have been widely explored.[32–34] Functionalization introduces active sites that improve the charge transfer between the surface and the target analyte. Recent studies have shown that chemical modification of TMDs can significantly tune their electronic and adsorption properties.[35–37] Nevertheless, most reported functionalization strategies focus on MoS_2 or other TMDs, while covalent functionalization of $MoSe_2$ for chemical sensing applications, particularly for nitroaromatic compounds, remains largely unexplored.[38] $MoSe_2$, a prominent member of the TMDs family, has recently attracted significant attention owing to its unique two-dimensional layered structure and exceptional electronic properties. As a single layer, $MoSe_2$ exhibits a direct bandgap, which makes it highly versatile for electronic and optoelectronic applications.[39–41]

Recent advances in flexible chemical sensors have explored the use of 2D materials and nanostructured composites for gas and nitroaromatic detection. Metal-doped MoS_2 nanoflowers demonstrated high SO_2 sensitivity at room temperature with DFT-confirmed charge transfer.[42] MXene/metal–organic framework-derived CuO nanohybrids enabled self-powered ammonia sensing with high sensitivity and flexibility,[43] while ZnO nanoflower–cellulose acetate/polyaniline composites improved ammonia detection *via* QCM devices.[44] Despite these advances, most sensors rely on pristine or doped materials, where interactions are dominated by physisorption, limiting selectivity. In this context, this work introduces the covalent functionalization of $MoSe_2$ with hydrogen-bond donor groups to enhance charge transfer and provide specific binding sites for nitroaromatic compounds, improving the sensitivity and selectivity compared to existing designs. However, despite these promising properties, $MoSe_2$ has been significantly less explored for nitroaromatic hydrocarbon sensing compared to other TMDs such as MoS_2, with only a few studies addressing its interactions with NAC molecules.[45–47] Its high electrical conductivity and strong surface activity make it a promising candidate for gas-sensing applications, particularly for the detection of volatile compounds. Alkyl halide molecules can alter the local electronic density, adjust the Fermi level, and promote specific interactions with electron-deficient analytes such as NACs. These modifications can potentially increase the sensitivity and selectivity for the detection of toxic or explosive compounds.[48,49] Importantly, although nitro groups are strong hydrogen bond acceptors, the deliberate introduction of hydrogen bond donor functional groups *via* covalent functionalization of $MoSe_2$ has not been reported for NAC sensing. Addressing this gap is a central focus of the present work.

In this study, we investigated the covalent functionalization of 1H-$MoSe_2$ using halogenated organic precursors, specifically iodoacetamide, iodoacetic acid, and iodomethanesulfonic acid. These alkyl halides are initially adsorbed physically on the substrate surface, followed by a chemical reaction in which the carbon–iodine bond is cleaved. The iodine atom is substituted by selenium in the $MoSe_2$ lattice, resulting in the formation of a stable carbon–selenium (C–Se) covalent bond. The newly introduced active sites tune the local electronic environment of the substrate, thereby enhancing its interactions with electron-deficient nitroaromatic compounds such as NB, *m*-NT, *p*-NT, TNP, *p*-NA, and *p*-NP. Using density functional theory (DFT) calculations, we systematically explored the adsorption behavior, charge redistribution, and electronic structural changes induced by functionalization and subsequent analyte binding. These results provide detailed insights into how C–Se covalent bonding modulates the sensing properties of $MoSe_2$, offering promising strategies for the design of high-performance two-dimensional sensors for environmental monitoring and security applications.

2. Methodology

Simulations were performed using the Quantum ESPRESSO package (v7.3).[50] The generalized gradient approximation in the PBE form was used to describe the exchange–correlation interactions between electrons.[51] GBRV high-throughput pseudopotentials were employed for all the atomic species.[52] The valence electron wavefunctions and charge densities were expanded in

a plane-wave basis set with kinetic energy cutoffs of 60 and 540 Ry, respectively, to ensure accurate convergence of the total energies and forces. A 5 × 5 $MoSe_2$ supercell was used in the functionalization and adsorption studies using a 4 × 4 × 1 Monkhorst–Pack *k*-point grid, which was sufficiently dense to ensure converged total energies and accurate geometry.[53] A denser 12 × 12 × 1 *k*-point grid was employed to ensure convergence of the density of states. Non-spin-polarized calculations were performed since the $MoSe_2$ monolayer and NAC compounds were not magnetic and contained no unpaired electrons. Test calculations confirmed that including spin polarization does not significantly affect the geometries, adsorption energies, or electronic properties.

For electronic optimization, the self-consistent field energy convergence was set to 10^{-6} Ry. Geometry relaxation was performed until the total energy variation was less than 10^{-6} Ry, and the residual atomic forces were less than 10^{-3} Ry $Bohr^{-1}$. A vacuum spacing (25 Å) was applied along the *z*-direction to avoid interactions between the periodic images of the $MoSe_2$ monolayer. For the adsorption studies, van der Waals interactions were accounted for using the DFT-D3 (version 4) method with Grimme's correction.[54,55] The functionalization of $MoSe_2$ with halogenated molecules was modeled at various adsorption sites (top, hollow, and bridge) to identify the most stable configurations. These computational parameters guarantee the stability and accuracy of the optimized geometry and electronic structure calculations for pristine and functionalized $MoSe_2$ systems.

3. Results and discussion

3.1. Structural model and adsorption sites

The pristine 1H-$MoSe_2$ monolayer consists of a single layer of molybdenum atoms sandwiched between two layers of selenium atoms, forming trigonal prismatic coordination. In the supercell, each lattice vector was expanded five times along the *a*- and *b*-directions, resulting in a periodic slab sufficiently large to accommodate adsorbed halogenated molecules without introducing artificial interactions between periodic images. The monolayer consisted of 25 Mo and 50 Se atoms. A vacuum of 25 Å was introduced in the direction perpendicular to the plane to avoid inter-plane interactions. The lateral dimensions of the simulation box are 16.63 Å × 16.63 Å. For hexagonal TMD monolayers, the optimized lattice preserves the $P6_3/mmc$ (No. 194) space-group symmetry. This supercell ensured adequate spatial separation between adsorbates and accurate electronic structure estimates by offering a suitable framework for the systematic investigation of covalent functionalization and adsorption using DFT. We investigated the physisorption of three halogenated molecules of interest, iodoacetamide (**1a**), iodoacetic acid (**1b**), and iodomethanesulfonic acid (**1c**). All three compounds contain an iodine atom but differ in their terminal functional groups, which can interact with the $MoSe_2$ surface through van der Waals forces, dipole–surface interactions, or weak coordination bonds. For each molecule, adsorption was explored at four distinct sites on the $MoSe_2$ monolayer, as depicted in Fig. 1. This systematic evaluation allowed the identification of the most energetically favorable adsorption configuration for each functionalized molecule, providing insight into the surface reactivity and potential sensing performance.

3.2. Evaluation of the energetic and electronic properties

After performing full geometric relaxation for each adsorption configuration, the energetic stability and local geometric characteristics of the resulting structures were examined. The adsorption energy (ΔE_{ads}) of each molecule was calculated using eqn (1).

$$\Delta E_{ads} = E_{adsorbate+MoSe_2} - E_{adsorbate} - E_{MoSe_2} \quad (1)$$

where $E_{adsorbate+MoSe_2}$ is the system energy, and E_{MoSe_2} and $E_{adsorbate}$ are the total energies of $MoSe_2$ and the adsorbate, respectively. A negative adsorption energy value indicates favorable adsorption. A similar treatment was used to determine the reaction energies between pristine $MoSe_2$ and the reactive intermediates.

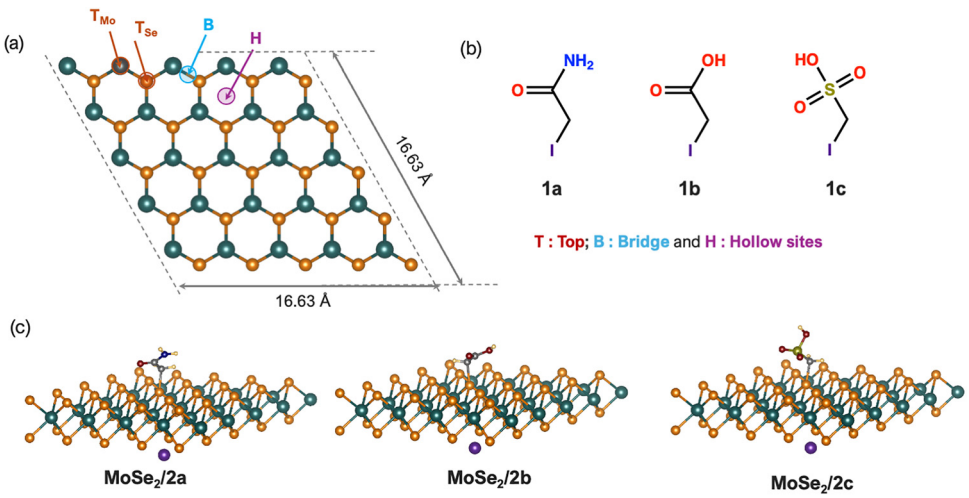

Fig. 1 (a) High-symmetry position examined for the adsorption of iodinated functional molecules, (b) chemical structures and corresponding reactive intermediates **1a–c**, and (c) relaxed geometries of functionalized surface MoS_2/**2a–c**.

We investigated the interactions between nitroaromatic compounds and functionalized $MoSe_2$ surfaces to assess their efficacy as chemical detectors. The targeted molecule was placed close to the modified surface of each structure, and the full system was relaxed. The interaction energies (ΔE_{int}) were calculated using eqn (2).

$$\Delta E_{int} = E_{NACs+fMoSe_2} - E_{NACs} - E_{fMoSe_2} \quad (2)$$

where E_{fMoSe_2} is the energy of the functionalized $MoSe_2$, E_{NAC} is the energy of a single isolated NAC molecule, and $E_{NAC/mMoSe_2}$ is the energy of the relaxed $fMoSe_2$ + NAC system.

A study of the charge density difference ($\Delta\rho$) was conducted to gain a better understanding of the interaction mechanism between the functionalized surface and target molecules. The differential charge density was computed using eqn (3):

$$\Delta\rho = \rho_{complex} - \rho_{fMoSe_2} - \rho_{target} \quad (3)$$

where $\rho_{complex}$ is the charge density of the complete system, ρ_{fMoSe_2} is the charge density of modified $MoSe_2$, and ρ_{target} is that of the target.

The recovery time (τ) represents the time required for an adsorbed molecule to desorb from the surface, indicating the reusability and response reversibility of the sensor.[56] This was calculated using the transition-state approximation theory,[57] which relates the desorption rate to the adsorption energy and temperature, and can be determined using eqn (4):

$$\tau = \nu^{-1}\exp(|\Delta E_{int}|/K_B T) \quad (4)$$

where T is the absolute temperature (K), k_B is Boltzmann's constant (8.617×10^{-5} eV K^{-1}), and ΔE_{int} is the interaction energy (eV). The attempt frequency is assumed to be 1×10^{12} Hz.

3.3. Physisorption analysis

The geometric configurations of the systems formed by the physical adsorption of three halogenated molecules, iodoacetamide (**1a**), iodoacetic acid (**1b**), and iodomethanesulfonic acid (**1c**), on the $MoSe_2$ surface were optimized for each considered site (Fig. 1b). The top and side views of the geometries obtained for each case are shown in Fig. S1 (see SI), highlighting the relative orientations of functional groups and iodine atoms with respect to the surface. After the full geometric relaxation of each configuration, the adsorbed structures were analyzed in terms of energy stability and local geometry. The minimum distances between the iodine and selenium atoms from the surface (Se–I) were extracted for each configuration to evaluate the adsorption proximity.

The adsorption energies showed that the interaction between adsorbates and the $MoSe_2$ surface was weak, which is characteristic of van der Waals-type interactions. As presented in Table 1, the energy values varied between −0.013 and −0.033 eV, confirming the physical adsorption. Among the different positions studied, the bridge configuration was systematically the most stable for all three molecules, with a minimum energy of −0.033 eV. This preference can be attributed to the better distribution of the interaction between the iodinated group and the surface.

Table 1 Physical and chemical adsorption energies of molecular functionalizers on $MoSe_2$ and their equilibrium positions in relaxed geometries

Systems	ΔE_{ads}/eV	d_{Se-X}/Å
$MoSe_2$/**1a**	−0.027[a]	4.59
	−0.031[b]	3.85
	−0.032[c]	3.79
	−0.018[d]	4.17
$MoSe_2$/**1b**	−0.021[a]	4.36
	−0.032[b]	3.86
	−0.033[c]	3.94
	−0.013[d]	5.12
$MoSe_2$/**1c**	−0.022[a]	3.94
	−0.018[b]	4.01
	−0.033[c]	4.08
	−0.029[d]	4.14
MoS_2/**2a**	−2.11	2.02
MoS_2/**2b**	−1.93	2.04
MoS_2/**2c**	−2.00	2.03

[a] T_{Se} position. [b] T_{Mo} position. [c] Bridge position. [d] Hollow position.

The minimum distances Se–I associated with the bridge configuration range from 3.79 Å for $MoSe_2$/**1a** to 4.08 Å for $MoSe_2$/**1c**, which confirms that the molecules remain at a reasonable distance from the surface without direct bond formation.

3.4. Covalent functionalization

The chemical functionalization of $MoSe_2$ using chemical reagents relies on a substitution mechanism involving breaking of the C–I bond. Under favorable conditions (thermal energy or assistance by surface defects), second-order nucleophilic substitution replaces the iodide ion with a nucleophilic doublet from the selenium atom exposed on the surface of $MoSe_2$, leading to the formation of a C–Se covalent bond and the stable grafting of the functional group. From the perspective of chemical adsorption, the formation of a C–Se covalent bond between the halogenated molecule and $MoSe_2$ constitutes a strong and irreversible interaction.

The optimized geometries of the functionalized $MoSe_2$ systems (Fig. 1c) revealed the successful formation of a stable C–Se covalent bond after cleavage of the carbon–iodine bond. This bond enhances the electronic integration of the molecule within the $MoSe_2$ lattice, potentially modifying its electronic structure and sensing properties. During the functionalization process, the released iodide ions were positioned beneath the surface to maintain overall charge neutrality, preventing the system from carrying a positive net charge, which could otherwise result in unphysical and unreliable adsorption energies. By preserving neutrality, the calculations provided a realistic assessment of the structural stability, electronic configuration, and potential detection performance of covalently functionalized $MoSe_2$–molecule complexes.

The results of chemical adsorption are summarized in Table 1, where for each molecule, the chemical adsorption energy ΔE_{ads} and the covalent distance C–Se, indicative of the strength of the bond formed, are indicated. The analysis of the results reflected significant stabilization of the system after the formation of the covalent bond Se–C. Among the studied reagents, compound (**1a**) exhibited the most negative adsorption energy (−2.11 eV), which

indicates a more favorable reaction than the other two compounds. This affinity can be attributed to the nature of the amide group, which promotes efficient alignment of the reactive carbon with the surface. Iodomethanesulfonic acid (**1c**) has an adsorption energy of −2.00 eV, while iodoacetic acid (**1b**) is slightly less attracted to the surface (−1.93 eV), although all energies remain within a narrow range, illustrating comparable reactivity for the three structures.

For the covalent distance Se–C, values vary very little: they range from 2.02 Å to 2.04 Å, which is consistent with the formation of a typical stable covalent bond between a selenium atom and a sp^3 carbon atom. These results suggest that these molecules can form robust chemical bonds with the $MoSe_2$ surface, while maintaining sufficient structural flexibility.

The different functional groups (*i.e.*, $-CONH_2$ in **1a**, $-CO_2H$ in **1b**, and $-SO_3H$ in **1c**) played a crucial role in the final functionality of the modified surface. Indeed, these groups can influence the polarity of the surface, the possibility of hydrogen interactions, and the molecular recognition ability in applications such as detection or catalysis. Thus, although the grafting mechanism remains identical, the chemical nature of the R group strongly modulates the physicochemical properties of the functionalized material.

3.5. Electronic properties

3.5.1. Band structures. The band structure of optimized $MoSe_2$ is shown in Fig. S2 in the SI file. This reveals a semiconductive character with a direct band gap at the K point. The bandgap energy was approximately 1.43 eV, which is in good agreement with the literature.[58,59] This agreement suggests that the optimized structure used in this study is reliable for the analysis of adsorption and detection properties. The electronic band structures of $MoSe_2$/**2a**, $MoSe_2$/**2b**, and $MoSe_2$/**2c** were also calculated to evaluate the effect of chemical functionalization on their electronic properties. The results in Fig. 2a show that the covalent introduction of these organic groups significantly changed the distribution of the electronic states, particularly around the Fermi level.

The electronic band structures of functionalized $MoSe_2$ materials show a significant reduction in the bandgap energy, ranging from 0.91 to 0.83 eV compared to pristine MoS_2 (E_g = 1.43 eV). This can be attributed to chemical functionalization, which leads to the formation of localized states near the Fermi level. These states manifest as flat bands in the band structure, indicating low dispersion and high localization, typically on the adsorbed molecule. This effect is more pronounced with highly polar groups, such as $-CO_2H$ and $-SO_3H$, which induce stronger perturbations in the electronic structure. Furthermore, the adsorbate is positively charged, and its charge is fully distributed over the supercell, which can introduce new charge carriers into the material. It is important to note that the material retains its semiconducting nature, which makes these functionalized systems promising candidates for chemical sensing applications based on band-structure modulation.

3.5.2. Density of states. The total electronic density of states was calculated for each system to better understand the impact of chemical functionalization on the overall distribution of the electronic levels. The curves in Fig. 2b allow the visualization of the possible appearance of new states introduced by functionalization and the evaluation of their influence on the electronic conductivity.

In the case of pristine $MoSe_2$, the DOS is distributed mainly within the range of −6 to 5 eV, whereas for functionalized $MoSe_2$, the distribution extends wider, ranging from −8 to 5 eV. This extension towards lower energies reflects the appearance of new deep electronic levels, originating from the orbitals of the functional molecule (amide, carboxyl, or sulfonate groups). The expanded DOS form indicates a broadening of the electronic response window, which is favorable for detection applications where sensitivity depends on subtle changes in the electronic profile. Overall, the three systems studied exhibited similar behavior in this shift tendency, confirming the systematic effect of covalent functionalization on the density of states of the base material.

3.5.3. Projected density of states. Further analysis was conducted by determining the projected density of states (PDOS) for each system to identify the contribution of the different atoms (Mo, Se, and C) to the electronic states close to the Fermi level and to determine the effect of chemical bond formation. Analysis of the PDOS showed that the major contributions around the Fermi level are essentially from the 4d and 2p orbitals of Mo and Se for pristine $MoSe_2$, respectively (Fig. 2c). A significant PDOS alteration was observed for the functionalized materials. A new intense peak appeared at the Fermi level ($E - E_F$ = 0 eV) in the three modified systems. This peak is due to the 2p orbital of the carbon from the adsorbates, confirming covalent Se–C formation. Concomitantly, the Se 2p orbital of the atom involved in the Se–C bond also exhibited an increased intensity at the same energy, probably arising from the positive charge introduced by the reactive intermediates. Moreover, a global shift in the PDOS was observed, particularly for the Mo 4d orbitals. This is due to functionalization, insofar as selenium bound to carbon locally influences the electron density of the adjacent molybdenum.

3.6. Sensing of nitroaromatics

3.6.1. Detection of nitrobenzene. To judge the effectiveness of the functionalized $MoSe_2$ surfaces as chemical detectors, we examined the interaction of the modified $MoSe_2$ with nitrobenzene, the simplest representative compound of the nitroaromatic family. For each structure, the targeted molecule was positioned near the altered surface and integral geometric optimization was performed, as shown in Fig. 3a.

The results summarized in Table 2 show that the $MoSe_2$/**2c** system exhibits the most stable interaction with nitrobenzene, displaying a more favorable adsorption energy of −2.07 eV and a minimum N–O···H hydrogen bonding distance of 1.64 Å, indicating a more powerful interaction between the surface and the target molecule.[60] This may be due to the strong acidity of the OH from the sulfonic group ($pK_a = -1.9$[61]) compared with that of the carboxylic acid or carbamide groups (pK_a of ∼4.7[62] and ∼15.1,[63] respectively).

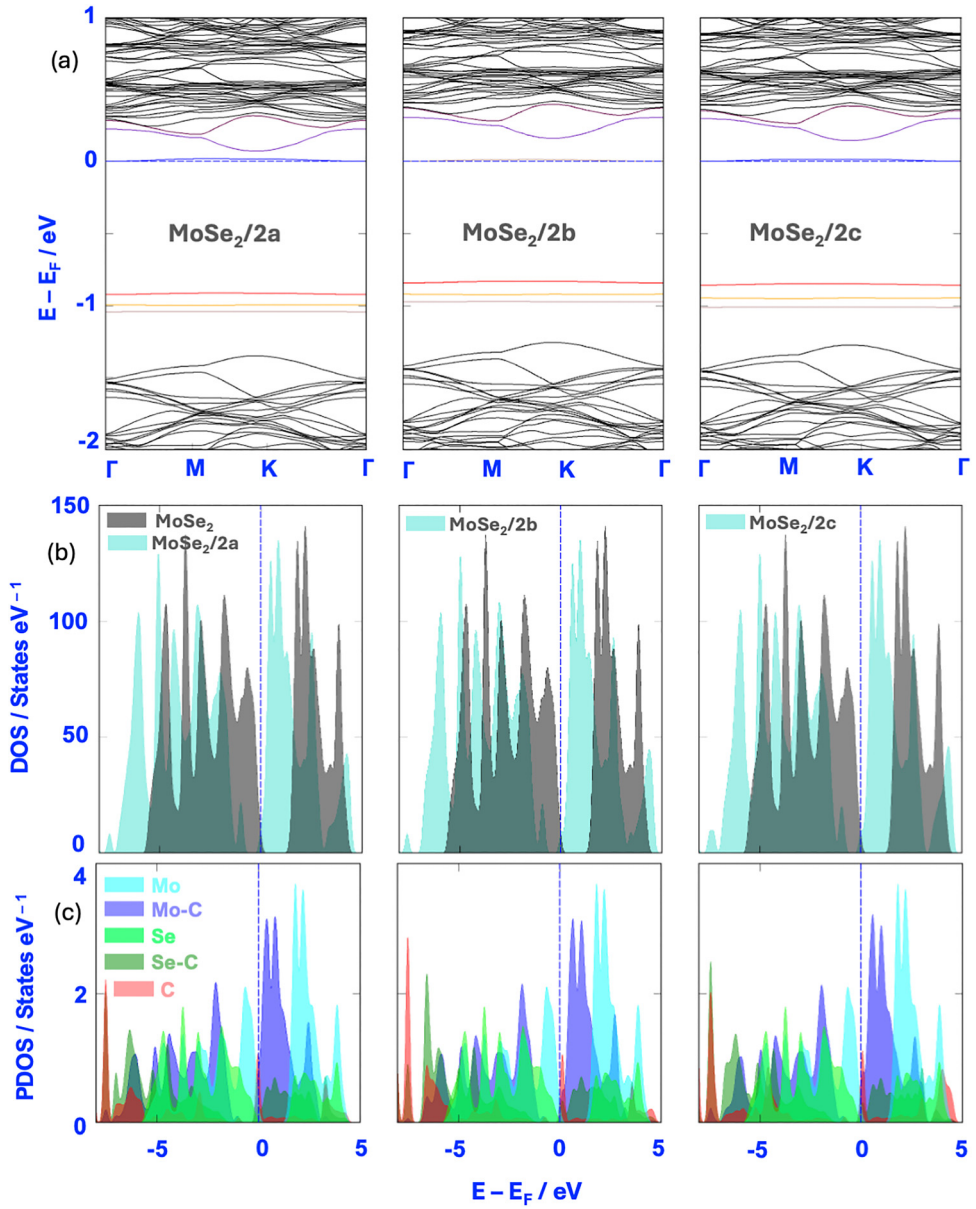

Fig. 2 The band structure (a), DOS (b), and PDOS (c) plots for $MoSe_2$/**2a**, $MoSe_2$/**2b**, and $MoSe_2$/**2c** show the bandgap and Fermi level for each material. The PDOS for each element is indicated by the color legend.

3.6.2. Detecting other NACs. To broaden the scope of the investigation beyond nitrobenzene, the $MoSe_2$/**2c** system was employed to explore its interactions with a wider range of nitroaromatic compounds. Additional molecules, including *m*-nitrotoluene, *p*-nitrotoluene, trinitrophenol, *p*-nitrophenol, and *p*-nitroaniline, were selected to represent the diverse structural and functional variations within the nitroaromatic family. The optimized geometries are shown in Fig. 3b. As summarized in Table 2, the calculated interaction energies span a relatively broad range (–1.95 to –2.26 eV), corresponding to N═O···H–O hydrogen bonds formed between the sulfonic acid moiety and the nitroaromatic adsorbates. The associated bond lengths vary from 1.61 to 1.66 Å, reflecting differences in interaction strength across the tested molecules. Among these, *p*-nitroaniline exhibited the most pronounced interaction. These results highlight the capability of the functionalized $MoSe_2$/**2c** material to interact strongly with a wide spectrum of nitroaromatic pollutants, underscoring its potential for comprehensive environmental monitoring of contaminated water and soil systems.

3.6.3. Charge density differences. A study of the charge density difference was conducted to better understand the interaction mechanism between the target molecules *p*-NT, *p*-NA, and *p*-NP and the functionalized $MoSe_2$/**2c** surface to visualize the charge transfer caused by adsorption, highlighting the areas of electron density loss and gain caused by the interaction between the two entities.

Fig. 4a shows a three-dimensional map of the charge density difference generated following the adsorption of analyte molecules

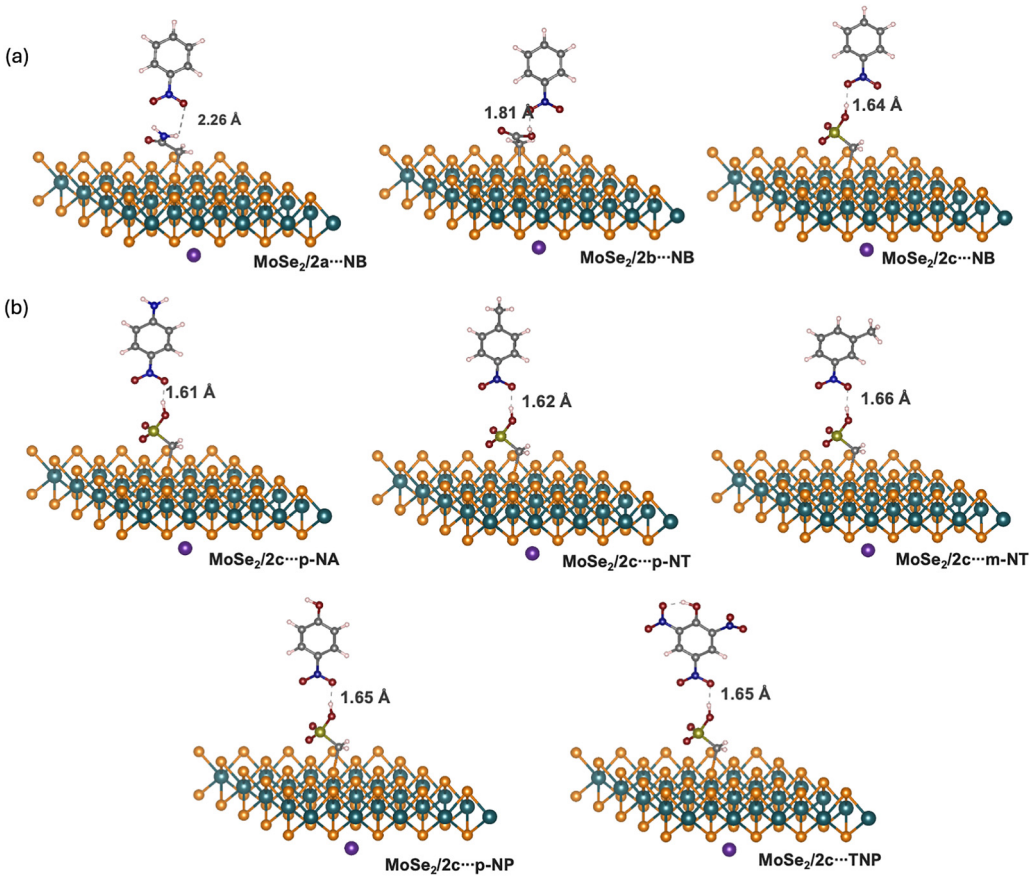

Fig. 3 Relaxed geometries of (a) NB···$MoSe_2$/**2a–c** and (b) other NACs interacting with $MoSe_2$/**2c** showing hydrogen bonds between the acidic O–H from the surface and O═N from the target NACs.

Table 2 Interaction energies of the target molecules with $MoSe_2$/**2a–c** *via* hydrogen bonding

Targets	Substrates	ΔE_{int}/eV	HB lengths/Å
NB	$MoSe_2$/**2a**	−1.84	N–O···H = 2.26
	$MoSe_2$/**2b**	−1.85	N–O···H = 1.81
	$MoSe_2$/**2c**	−2.07	N–O···H = 1.64
m-NT	$MoSe_2$/**2c**	−2.03	N–O···H = 1.66
p-NT		−2.08	N–O···H = 1.62
TNP		−1.95	N–O···H = 1.65
p-NA		−2.26	N–O···H = 1.61
p-NP		−2.09	N–O···H = 1.65

(*p*-NT, *p*-NP, and *p*-NA) on the functionalized $MoSe_2$/**2c** surface. The blue areas corresponding to the electron-depleting regions (charge density loss) are located mainly around the oxygen atoms of the $–NO_2$ group of the analyte molecules, as well as partly around the sulfonic acid hydrogen. This depletion indicates charge donation from these regions to the functionalized surface. In contrast, the yellow areas indicate charge-accumulation regions (charge density gain), which are visible around the bonds between the functional groups of the two species, between the oxygen or nitrogen atoms of the nitro group, and between the sulfur and oxygen atoms of the sulfonic acid. The complementary charge distribution zones confirm the existence of partial charge transfer between the target molecules and the sensing surface. This phenomenon is a direct indicator of chemisorption interactions, which is consistent with the high adsorption energies obtained previously.

3.6.4. Partial charges. To better understand the electronic effects of the interactions between the functionalized surface and the NACs, partial charges were determined for the $MoSe_2$/**2c** systems interacting with *p*-NT, *p*-NP, and *p*-NA by analyzing the Löwdin population (Fig. 4b). This was used to estimate the net charge transfers between the target molecules and the modified surface and to evaluate the nature of the interactions at the atomic scale. We focused on the main atoms involved in the interaction, notably the S, O, N, and H atoms.

The acidic hydrogen from SO_3H exhibits a negative charge variation ($\sim$−0046*e*), reflecting electron gain due to hydrogen bonding with the electronegative O atom. The sulfur atom displays a positive charge change ($\sim$+0.016*e*), indicating local electron loss. The hydrogen-bonded oxygen of SO_3H is negatively charged because of charge accumulation due to the strengthening of the O–H bond during interaction, while the other two oxygens of the SO_3H group have partial charges of ($\sim$−0.026*e*) and ($\sim$−0.006*e*). This asymmetry reflects the uneven distribution of the electrostatic field, which is likely related to the spatial orientation of the target molecules. Regarding the $–NO_2$

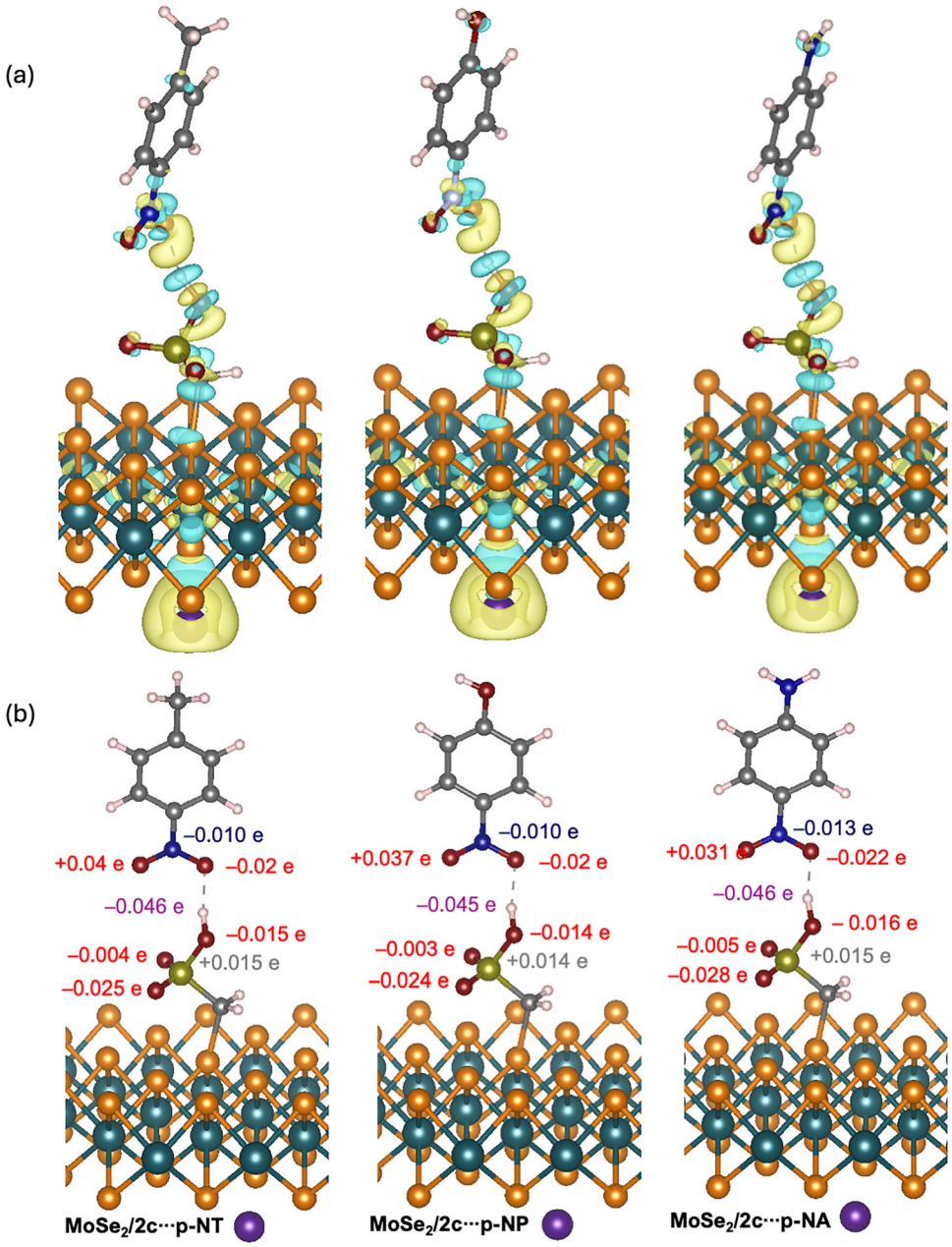

Fig. 4 (a) Electronic density differences and (b) Löwdin partial charges for $MoSe_2$/**2c** interacting with *p*-NT, *p*-NP, and *p*-NA target molecules. The charge density differences were plotted at a density isovalue of 2.5 × 10^{-3}e $Bohr^{-3}$.

grouping of molecules, the nitrogen atom (N) gains a small number of electrons (−0.010 and −0.013*e*), which is typical for its role in stabilizing the charge by resonance in $–NO_2$. Among the two oxygen atoms, the one involved in hydrogen bonding gains a slightly higher charge (∼–0.020*e*), whereas the other loses electrons (∼+0.031*e*), suggesting an internal reorganization of the electron cloud within the group $–NO_2$.

These partial load variations indicate that the hydrogen bond between the H of SO_3H and the O of NO_2 is the main anchor point of the interaction. Electron transfer is oriented from the acid group to the nitro group, which confirms the electrophilic nature of the latter. The entire transfer was consistent with a chemisorption interaction stabilized by local electron polarization, thus enhancing the sensitivity and selectivity of the sensor.

Charge density difference and partial charge analyses provide a direct link between the adsorption strength and sensing response. The significant charge redistribution induced by NAC adsorption, particularly through hydrogen bonding between the SO_3H functional group and the $–NO_2$ moieties, leads to modulation of the local carrier concentration near the Fermi level of the functionalized $MoSe_2$ surface. The magnitude of the calculated charge transfer, as revealed by the Löwdin population analysis, quantitatively reflects the degree of electronic perturbation induced by the adsorbates. Therefore, stronger

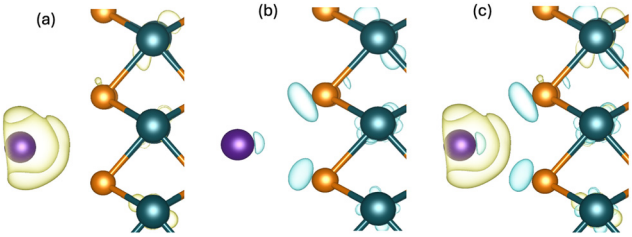

Fig. 5 Charge density differences for positive (a), negative (b), and positive and negative (c) charges participating in the pnictogen-type bond between iodine and selenium.

adsorption energies accompanied by larger charge transfer are expected to result in more pronounced conductivity variations. Although explicit charge transport calculations were not performed, the observed charge redistribution served as a reliable quantitative indicator of the change in conductivity, which is consistent with the operating principle of resistive 2D material-based sensors.

3.6.5. Halogen bonding. Furthermore, the iodide atom interacts with the bottom surface through a pnictogen-type bond involving the σ-hole located on the iodine atom and localized excess electron density on the adjacent selenium atoms (Fig. 5).[64–66] This specific interaction contributed to the overall stabilization of the adsorption configuration. Owing to its high polarizability, the iodine atom exhibits significant deformation of its outermost electron cloud, resulting in distinct regions of positive and negative electrostatic potentials. As illustrated in Fig. 5a, the positive region (yellow) corresponds to the σ-hole formed along the extension of the C–I bond, whereas the negative region (blue, Fig. 5b) represents the area of electron accumulation. The alignment of the σ-hole on iodine with the negatively charged selenium sites facilitates an electrostatically driven attraction, which is characteristic of a pnictogen bonding interaction. This behavior highlights the crucial role of halogen and pnictogen polarization in modulating the surface adsorption processes and tuning the electronic coupling between the adsorbate and the substrate. The molybdenum atom presents an area of charge depletion and gain perpendicular to the axis of the I···Se non-covalent interaction.

3.7. Recovery times

The recovery times as a function of temperature for $MoSe_2$/**2c** with three target molecules is studied (Table 3). The value, calculated from the adsorption energies, indicated strong temperature dependence for all target molecules. At 298 K, these values were extremely high (on the order of 10^{19}–10^{22} h), reflecting the stable chemical adsorption of NACs on the functionalized surface.

At higher temperatures, the recovery times decreased significantly, reaching 10^{10}–10^{13} and 10^{5}–10^{7} h, confirming the thermally activated nature of the desorption process at 400 and 500 K, respectively. The *p*-NA exhibits a distinct behavior: although its adsorption energy is the highest (2.26 eV), the estimated recovery time of approximately 2.1×10^{7} h suggests faster desorption at high temperatures, which could result from local reorganization or partial relaxation of the bond between the NH_2 group and the surface.

Table 3 Recovery times computed from the interaction energies between the target molecules and the sensing surface

		Recovery times/h		
Entry	Systems	298 K	398 K	498 K
1	$MoSe_2$/**2c**···*p*-NT	4.2×10^{19}	6.1×10^{10}	3.1×10^{5}
2	$MoSe_2$/**2c**···*p*-NA	4.6×10^{22}	1.1×10^{13}	2.1×10^{7}
3	$MoSe_2$/**2c**···*p*-NP	6.2×10^{19}	8.1×10^{10}	3.9×10^{5}

These results clearly show that an increase in temperature promotes the destruction of the adsorbed molecules and significantly reduces the recovery time. However, at relatively low temperatures, analyte retention indicates that detection relies mainly on strong chemisorption, providing the system with excellent sensitivity but limiting its ability to quickly regenerate. Among the three molecules, *p*-NA exhibited the strongest interaction with the functionalized surface, confirming its ability to selectively and stably detect the modified $MoSe_2$.

4. Conclusions

This study demonstrates that the chemical functionalization of $MoSe_2$ with halogenated organic groups containing hydrogen-bond donor functionalities (–$CONH_2$, –CO_2H, and –SO_3H) markedly enhances its potential as a sensing material for detecting nitroaromatic pollutants. The introduction of these functional groups significantly strengthens the adsorption interactions, with the chemical binding energies exceeding the physical adsorption energies by nearly two orders of magnitude. Electronic structure analyses revealed pronounced modifications in the conduction band and a notable bandgap reduction (approximately 0.5 eV), confirming the strong electronic coupling between $MoSe_2$ and adsorbed nitroaromatics. The adsorption energies in the range of –1.84 to –2.26 eV and the corresponding charge transfer patterns indicate high sensitivity, particularly for the $MoSe_2$/**2c** system. These findings underscore the potential of functionalized $MoSe_2$ as an efficient and tunable platform for detecting nitroaromatic contaminants such as NB, *m*-NT, *p*-NT, TNP, *p*-NP, and *p*-NA. Overall, this work provides valuable insights into the rational design of two-dimensional materials for environmental monitoring and pollutant detection in complex ecosystems.

Author contributions

RH: investigation, conceptualization, and data curation, writing – original draft; SB: investigation, data curation, writing – original draft; SBA: writing – review & editing; SR: writing – review & editing; NR: methodology, supervision, validation, writing – review & editing.

Conflicts of interest

The authors declare no conflict of interest.

Data availability

Data for the paper can be found at the Harvard Dataverse: https://doi.org/10.7910/DVN/U2Q0PA.

Supplementary information (SI): equilibrium positions for the physical adsorption of the iodated chemical modifiers on atop, bridge and hollow positions with the respective equilibrium distance to surface (Fig. S1) and band structure of the pristine $MoSe_2$ (Fig. S2) that supports the results presented in the main manuscript. See DOI: https://doi.org/10.1039/d5ma01255d.

Acknowledgements

For computer time, this research used Shaheen III, managed by the Supercomputing Core Laboratory at King Abdullah University of Science & Technology (KAUST) in Thuwal, Saudi Arabia (project ref. k10103).

References

1 M. Fabin, M. Łapkowski and T. Jarosz, *Appl. Sci.*, 2023, **13**, 3991.
2 P. Ghosh, S. K. Saha, A. Roychowdhury and P. Banerjee, *Eur. J. Inorg. Chem.*, 2015, 2851–2857.
3 G. Awasthi, R. Sharma, S. Sundarrajan, S. Ramakrishna and P. Kumar, *Polymers*, 2022, **14**, 4643.
4 K. Anichina, N. Lumov, V. Bakov, D. Yancheva and N. Georgiev, *Molecules*, 2024, **29**, 3475.
5 N. Pino and G. Peñuela, *Int. Biodeterior. Biodegrad.*, 2011, **65**, 827–831.
6 K. Tao, H. Tian, Z. Wang, X. Shang, J. Fan, M. Megharaj, J. Ma, H. Jia and W. He, *Chemosphere*, 2023, **311**, 137116.
7 A. Chowdhury and P. S. Mukherjee, *J. Org. Chem.*, 2015, **80**, 4064–4075.
8 Y. Wang, A. La, C. Brückner and Y. Lei, *Chem. Commun.*, 2012, **48**, 9903–9905.
9 X. Sun, Y. Wang and Y. Lei.
10 A. Deshmukh, S. Bandyopadhyay, A. James and A. Patra, *J. Mater. Chem. C*, 2016, **4**, 4427–4433.
11 T. Jadoon, T. Mahmood and K. Ayub, *J. Mol. Liq.*, 2020, **306**, 112878.
12 J. Yang, L. Xia, Z. Lin, Z. Tang, G. Li and Y. Hu, *Chin. Chem. Lett.*, 2019, **30**, 638–642.
13 M. Kaur, S. K. Mehta and S. K. Kansal, *Spectrochim. Acta, Part A*, 2017, **180**, 37–43.
14 K.-S. Ju and R. E. Parales, *Microbiol. Mol. Biol. Rev.*, 2010, **74**, 250–272.
15 T. Kokulnathan, A. I. Jothi, S.-M. Chen, G. Almutairi, F. Ahmed, N. Arshi and B. AlOtaibi, *J. Environ. Chem. Eng.*, 2021, **9**, 106310.
16 Y. Ren, Z. Ma, T. Gao and Y. Liang, *Molecules*, 2023, **28**, 4481.
17 J. P. Cachaneski-Lopes, F. Hawthorne, C. F. Woellner, T. L. Nelson, R. C. Hiorns, C. F. O. Graeff, D. Bégué and A. Batagin-Neto, *ACS Omega*, 2025, **10**, 31908–31920.
18 R. Sainda, D. Chodvadiya, I. Zgłobicka, K. J. Kurzydłowski and P. K. Jha, *J. Mol. Liq.*, 2024, **409**, 125389.
19 A. L. Desai, N. P. Patel, J. H. Parikh, K. M. Modi and K. D. Bhatt, *J. Fluoresc.*, 2022, **32**, 483–504.
20 S. Sarfaraz, M. Yar, A. Ali Khan, R. Ahmad and K. Ayub, *J. Mol. Liq.*, 2022, **352**, 118652.
21 D. Paul, A. Vaidyanathan, U. Sarkar and B. Chakraborty, *Struct. Chem.*, 2021, **32**, 2259–2270.
22 L. Liu, X. Chen, J. Qiu and C. Hao, *Dalton Trans.*, 2015, **44**, 2897–2906.
23 J. P. Perdew, K. Burke and M. Ernzerhof, *Phys. Rev. Lett.*, 1996, **77**, 3865–3868.
24 H. Sajid, M. Asif, K. Ayub, M. A. Gilani, M. S. Akhter and T. Mahmood, *Surf. Interfaces*, 2021, **27**, 101587.
25 N. Nabeela, M. A. Hashmi, A. N. S. Saqib, A. Kamran and A. Lakhani, *RSC Adv.*, 2024, **14**, 30116–30126.
26 S. Baachaoui, R. Hajlaoui, S. B. Aoun, A. Fortunelli, L. Sementa and N. Raouafi, *Nanotechnology*, 2024, **35**, 425501.
27 X. Chen and B. Chen, *Environ. Sci. Technol.*, 2015, **49**, 6181–6189.
28 X. Lu, H. Qi, X. Zhang, Z. Xue, J. Jin, X. Zhou and X. Liu, *Chem. Commun.*, 2011, **47**, 12494–12496.
29 S. Ganesan, T. Kokulnathan and A. Palaniappan, *ACS Appl. Nano Mater.*, 2025, **8**, 7004–7014.
30 S. Baachaoui, S. Aldulaijan, F. Raouafi, R. Besbes, L. Sementa, A. Fortunelli, N. Raouafi and A. Dhouib, *RSC Adv.*, 2021, **11**, 7070–7077.
31 J. Gupta, D. S. S. Kandkuri and S. Rattan, *J. Mater. Sci.*, 2024, **59**, 3689–3710.
32 G. Gu, Z. Cui, X. Du, P. He, C. Rong, H. Tao, G. Wei and Y. Xi, *Adv. Funct. Mater.*, 2024, **34**, 2408367.
33 T. Zahra, U. Javeria, H. Jamal, M. M. Baig, F. Akhtar and U. Kamran, *Anal. Chim. Acta*, 2024, **1316**, 342880.
34 S. Ambreen, D. K. Gupta, H. Kumar, A. Sharma, S. Arun, S. Kumar, A. Saraswat and A. K. Mishra, *Luminescence*, 2025, **40**, e70273.
35 R. Hajlaoui, S. Baachaoui, S. Ben Aoun, S. Ridene and N. Raouafi, *ACS Omega*, 2024, **9**, 37953–37964.
36 D. Voiry, A. Goswami, R. Kappera, C. de C. C. e Silva, D. Kaplan, T. Fujita, M. Chen, T. Asefa and M. Chhowalla, *Nat. Chem.*, 2015, **7**, 45–49.
37 D. Voiry, A. Mohite and M. Chhowalla, *Chem. Soc. Rev.*, 2015, **44**, 2702–2712.
38 D. O. Li, M. S. Gilliam, X. S. Chu, A. Yousaf, Y. Guo, A. A. Green and Q. H. Wang, *Mol. Syst. Des. Eng.*, 2019, **4**, 962–973.
39 D. Zhang, H. Guan, W. Zhu, J. Yu, H. Lu, W. Qiu, J. Dong, J. Zhang, Y. Luo and Z. Chen, *Opt. Express*, 2017, **25**, 28536–28546.
40 A. S. Murali, S. Lekshmi and B. Saraswathyamma, *Tungsten*, 2025, **7**, 215–242.
41 S. Kandar, K. Bhatt, N. Kumar, A. K. Kapoor and R. Singh, *ACS Appl. Nano Mater.*, 2024, **7**, 8212–8220.
42 D. Zhang, J. Wu, P. Li and Y. Cao, *J. Mater. Chem. A*, 2017, **5**, 20666–20677.
43 D. Wang, D. Zhang, Y. Yang, Q. Mi, J. Zhang and L. Yu, *ACS Nano*, 2021, **15**, 2911–2919.
44 D. Zhou, Z. Kang, X. Liu, W. Yan, H. Cai, J. Xu and D. Zhang, *Sens. Actuators, B*, 2023, **392**, 134072.

45 A. Mirzaei, M. Alizadeh, H. R. Ansari, M. Moayedi, Z. Kordrostami, H. Safaeian, M. H. Lee, T. Kim, J. Kim, H. W. Kim and S. S. Kim, *Nanotechnology*, 2024, **35**, 332002.
46 S. Paria and P. Maity, *ACS Appl. Nano Mater.*, 2024, **7**, 16516–16524.
47 Aneesha and M. S. Mehata, *Mater. Res. Bull.*, 2025, **185**, 113287.
48 E. X. Yan, M. Cabán-Acevedo, K. M. Papadantonakis, B. S. Brunschwig and N. S. Lewis, *ACS Mater. Lett.*, 2020, **2**, 133–139.
49 A. Vaidyanathan, S. Lakshmy, G. Sanyal, S. Joseph, N. Kalarikkal and B. Chakraborty, *Appl. Surf. Sci.*, 2021, **550**, 149395.
50 P. Giannozzi, S. Baroni, N. Bonini, M. Calandra, R. Car, C. Cavazzoni, D. Ceresoli, G. L. Chiarotti, M. Cococcioni, I. Dabo, A. D. Corso, S. Fabris, G. Fratesi, S. de Gironcoli, R. Gebauer, U. Gerstmann, C. Gougoussis, A. Kokalj, M. Lazzeri, L. Martin-Samos, N. Marzari, F. Mauri, R. Mazzarello, S. Paolini, A. Pasquarello, L. Paulatto, C. Sbraccia, S. Scandolo, G. Sclauzero, A. P. Seitsonen, A. Smogunov, P. Umari and R. M. Wentzcovitch, *J. Phys.: Condens. Matter*, 2009, **21**, 395502.
51 J. P. Perdew, K. Burke and M. Ernzerhof, *Phys. Rev. Lett.*, 1996, **77**, 3865–3868.
52 K. F. Garrity, J. W. Bennett, K. M. Rabe and D. Vanderbilt, *Comput. Mater. Sci.*, 2014, **81**, 446–452.
53 P. Wisesa, K. A. McGill and T. Mueller, *Phys. Rev. B*, 2016, **93**, 155109.
54 S. Grimme, A. Hansen, J. G. Brandenburg and C. Bannwarth, *Chem. Rev.*, 2016, **116**, 5105–5154.
55 S. Grimme, J. Antony, S. Ehrlich and H. Krieg, *J. Chem. Phys.*, 2010, **132**, 154104.
56 S. Baachaoui, S. Aldulaijan, L. Sementa, A. Fortunelli, A. Dhouib and N. Raouafi, *J. Phys. Chem. C*, 2021, **125**, 26418–26428.
57 J.-H. Li, J. Wu and Y.-X. Yu, *Appl. Surf. Sci.*, 2021, **546**, 149104.
58 K.-A. N. Duerloo, M. T. Ong and E. J. Reed, *J. Phys. Chem. Lett.*, 2012, **3**, 2871–2876.
59 P. P. Hankare, P. A. Chate, S. D. Delekar, V. M. Bhuse, M. R. Asabe, B. V. Jadhav and K. M. Garadkar, *J. Cryst. Growth*, 2006, **291**, 40–44.
60 T. Steiner, *Angew. Chem., Int. Ed.*, 2002, **41**, 48–76.
61 D. B. Roitman, J. McAlister and F. L. Oaks, *J. Chem. Eng. Data*, 1994, **39**, 56–60.
62 H. S. Harned and R. W. Ehlers, *J. Am. Chem. Soc.*, 1933, **55**, 652–656.
63 G. E. K. Branch and J. O. Clayton, *J. Am. Chem. Soc.*, 1928, **50**, 1680–1686.
64 M. Weingarth, N. Raouafi, B. Jouvelet, L. Duma, G. Bodenhausen, K. Boujlel, B. Schoellhorn and P. Tekely, *Chem. Commun.*, 2008, 5981–5983.
65 G. Cavallo, P. Metrangolo, T. Pilati, G. Resnati and G. Terraneo, in *Halogen Bonding I: Impact on Materials Chemistry and Life Sciences*, ed. P. Metrangolo and G. Resnati, Springer International Publishing, Cham, 2015, pp. 1–17.
66 E. Rahali, M. Zouaghi, J. Sanz, N. Raouafi and Y. Arfaoui, *J. Comput. Chem.*, 2023, **44**, 1426–1436.